Small Science

small science

www.small-science-journal.com

RESEARCH ARTICLE OPEN ACCESS

Unveiling Non-classical Pathways in Copper Electrodeposition via In Situ Electrochemical Liquid-Cell Transmission Electron Microscopy

Monica Parpal[1,2] | Layrton José Souza da Silva[3,4] | Daniel Torres[1] | Aleksei Leontev[1] | Mohamed El Marini[2] | Sorour Semsari Parapari[4] | Sašo Šturm[3,4,5] | Jon Ustarroz[1,2]

[1]ChemSIN – Chemistry of Surfaces, Interfaces and Nanomaterials, Université libre de Bruxelles Campus de la Plaine, Brussels, Belgium | [2]SUME – Sustainable Materials Engineering, Vrije Universiteit Brussel, Brussels, Belgium | [3]Jožef Stefan International Postgraduate School, Ljubljana Slovenia | [4]Department for Nanostructured Materials, Jožef Stefan Institute, Ljubljana, Slovenia | [5]Department for Geology, Faculty for Natural Sciences and Engineering, University of Ljubliana, Ljubljana, Slovenia

Correspondence: Jon Ustarroz (jon.ustarroz@ulb.be)

Received: 1 April 2026 | **Revised:** 16 May 2026 | **Accepted:** 9 June 2026

Keywords: copper | crystal growth | electrochemistry | in situ electrochemical liquid-cell transmission electron microscopy | nanoparticle dynamics | non-classical growth pathways

ABSTRACT

Electrochemical nucleation and growth are traditionally described by classical atom-by-atom deposition models, yet the nanoscale dynamics governing phase formation at electrochemical interfaces remain poorly understood. Here, we directly visualize copper electrodeposition on glassy carbon by combining in situ electrochemical liquid-cell transmission electron microscopy (EC-TEM) with cyclic voltammetry, enabling direct correlation between global electrochemical signals and particle-resolved structural dynamics. Real-time imaging reveals that nanoparticle formation proceeds through a complex interplay of classical and non-classical pathways. Beyond radial and dendritic growth, we observe a range of particle-level processes, including mobility, coalescence, ripening-like mass exchange, and discrete relocation events, reflecting coupled transport and morphological transformation at the nanoscale. Quantitative tracking of individual nanoparticles reveals localized mass-transfer processes, including near one-to-one ripening dynamics and particle–particle interactions that redistribute material without producing a clear signature in the voltammetric response. These findings demonstrate that processes such as ripening, coalescence, and structural rearrangements can proceed without a discernible signature in the global electrochemical response. By bridging in situ nanoscale imaging with electrochemical analysis, this work provides direct mechanistic insight into early-stage electrochemical phase formation and highlights the dynamic nature of metal growth at electrochemical interfaces.

1 | Introduction

Electrodeposition is a fundamental and versatile technique for materials synthesis, valued for its control over key reaction parameters, such as potential, current, and time [1, 2]. As a result, it enables the fabrication of structures ranging from atomic clusters to complex three-dimensional architectures [1, 3–5]. Moreover, the method enables the direct growth of nanostructures on conductive substrates, thereby ensuring reliable electrical contact for electronic [1, 6] and catalytic devices [4, 5, 7]. The final morphology of electrodeposited metals, however, depends on both kinetic and thermodynamic parameters, which govern the underlying electrochemical nucleation and growth (EN&G) processes [8–10].

EN&G at the solid–liquid interface is a complex and heterogeneous phenomenon that involves a sequence of simultaneous

events, including the adsorption of precursor species (adatoms) onto the electrode surface, surface diffusion, nucleation, and subsequent growth of new phases [9–15]. While classical models typically assume atom-by-atom growth (direct attachment) with immobile nuclei on the substrate [9, 13], growing evidence indicates that such models do not fully capture nanoscale behavior [12, 15–24]. Instead, the complexity of this phenomenon points to what are known as non-classical pathways, which have been more deeply studied in homogenous nucleation and growth in liquid phase [16, 25, 26]. In this work, we use the term "non-classical pathways" in a phenomenological sense to describe phase transformations that deviate from the classical picture of immobile nuclei growing or dissolving exclusively by direct atom-by-atom (det)attachment at the particle/electrolyte interface. These pathways include lateral particle motion, aggregation and coalescence, ripening-like mass redistribution, particle restructuring, and division [12, 18, 22–24]. The term does not imply that a single mechanism is uniquely proven in each case, but rather that the observed deposit evolution cannot be fully described by classical, spatially uniform direct-attachment models alone [19, 27]. These mechanisms are strongly influenced by local surface heterogeneity, which governs nucleation, growth, and mobility at the particle level [11, 28–31]. Crucially, this local diversity is often masked in conventional macroscale measurements, which only provide an averaged response of the system.

To overcome these limitations, in situ techniques have recently provided sensitive platforms for probing single-nanoparticle electrochemistry and tracking phase formation with high temporal resolution. In particular, wide-field optical microscopies have pioneered the real-time imaging of reaction footprints and gas evolution at the single-entity level [32–35]. Complementing these optical approaches, in situ electrochemical liquid-cell transmission electron microscopy (EC-TEM) has become a powerful technique to probe electrodeposition with nanoscale spatial and temporal resolution [36–44]. This technique enables direct visualization of particle motion [45, 46], structural transformations [47], and dendrite formation in real time [36, 40, 41, 48–50]. Nevertheless, in situ EC-TEM experiments face challenges, primarily due to electron-beam-induced artifacts; for instance, electron-beam radiolysis of the solvent can generate radicals that alter reaction chemistry [51–54]. Furthermore, the confined geometry of the liquid cell restricts mass transport, while the deformation (bulging) of the electron-transparent windows can significantly compromise image resolution [55–57]. However, advances in cell design, imaging strategies, and analysis workflows have significantly improved the reliability and quantitative capabilities of in situ EC-TEM studies [53, 55, 58–60].

In this work, we combine in situ EC-TEM with cyclic voltammetry (CV) to study the dynamic behavior of copper EN&G on a carbon substrate. By correlating the global electrochemical signals with nanoscale-resolved real-time imaging, we directly observe both classical and non-classical pathways of phase evolution. Our observations provide direct visual and in situ evidence that growth during cathodic polarization is not limited to simple atom-by-atom attachment and reveal complex restructuring events that lack a detectable voltammetric signature. Furthermore, by quantitatively tracking individual nanoparticles, we characterize the nature of their mobility during the electrodeposition process.

These observations offer a fundamental local view of the complex dynamics and structural evolution of nanoparticles during electrodeposition. The ability to resolve such localized and transient events is essential for understanding the mechanisms governing the growth, stability, and degradation of nanomaterials.

2 | Results and Discussion

2.1 | Optimization of In Situ EC-TEM & Cyclic Voltammetry Scan: Establishing Initial Conditions

Careful optimization of in situ EC-TEM conditions was required to enable high-resolution, real-time observation of electrochemical processes at the nanoscale. Details on reagents, chip specifications, and microfluidic dynamics are provided in the Experimental Section.

To enhance resolution, the electrolyte thickness was reduced by generating an oxygen (O_2) bubble at +0.8 V for 5 s (hereinafter, all potentials are given with respect to the Pt reference electrode of the liquid-cell chip. Calibration measurements against an Ag/AgCl reference electrode yielded an open-circuit potential difference of approximately +0.52 V, corresponding approximately to $E_{vs.Ag/AgCl} \approx E_{vs.Pt} + 0.52\ V$ and $E_{vs.SHE} \approx E_{vs.Pt} + 0.72\ V$).

The resulting bubble effectively displaced the bulk electrolyte, thinning the liquid layer to approximately 50 nm. This physical displacement mechanism creates a confined liquid film surrounding the electrode surface while maintaining the concentration of electroactive Cu^{2+} species in the electrolyte. Although some degree of surface evolution of the glassy carbon electrode under anodic polarization cannot be excluded, the short anodic pulse used for bubble generation did not prevent subsequent copper electrodeposition and nanoparticle growth. This confined liquid geometry is crucial for achieving the high spatial and temporal resolution required for our experiments (Section 2.1) [61–63].

The critical role of this O_2 bubble was first identified in preliminary experiments (Section S3.1, Supporting Information), where its presence enabled a transition from an unobservable surface to clearly visible particles. Once clear nanoscale visualization was confirmed, a stability test was performed to ensure that the electron beam did not induce structural changes or unintended deposition. This test was performed with the 1 mM $CuSO_4$ and 10 mM H_2SO_4 solution already in the system, confirming that no beam-induced growth, dissolution, particle movement, restructuring, or ripening occurred under these experimental conditions (Section S5, Supporting Information).

Finally, a cleaning step (+0.5 V for 60 s) was performed to dissolve residual Cu particles from previous experiments. While the chronoamperometric (CA) profile and the corresponding in situ transmission electron microscopy (TEM) images (Figure 1) demonstrate that this step effectively clears the majority of the surface, certain Cu particles persistently resisted dissolution. These remaining particles were found to be localized around a specific GC surface heterogeneity (Figure 1b, outline). In our preliminary experiments, we observed that areas of the

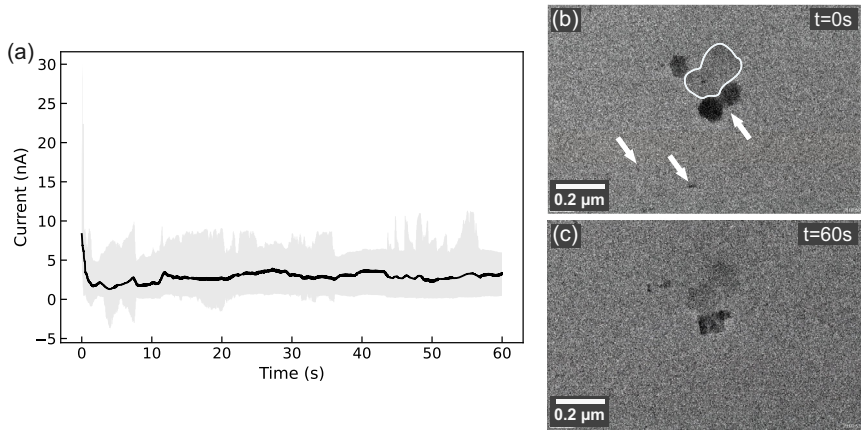

FIGURE 1 | Correlated electrochemistry and in situ TEM of Cu particle dissolution. (a) Current signal during a +0.5 V oxidative step. The solid line and shaded area represent the processed signal and noise estimation, respectively (see Section S3.2 for signal processing details, Supporting Information). (b,c) Representative in situ EC-TEM images of the working electrode surface: (b) before dissolution; arrows indicate Cu particles, and the outline highlights a specific surface feature, and (c) after dissolution.

surface that appeared pristine often exhibited no observable deposition under potential bias. Consequently, the specific area of observation was selected based on the presence of residual copper particles. These sites serve as a visual indicator of high surface activity zones, ensuring the reliable capture of electrodeposition phenomena during the subsequent experiments.

Following the CA step, an initial CV (protocol detailed in Section 4.3) was performed to establish a stable and trackable starting surface for the subsequent analysis (Figure 2a and Video S1). This first scan establishes the system's initial electrochemical response and ensures that any nuclei below the TEM detection threshold (~10 nm) grow into observable nanoparticles. As a result, the electrode surface exhibited a heterogeneous distribution of Cu nanoparticles (Figure 2b–e). The variations in size and spatial arrangement arising from intrinsic surface heterogeneity served as an essential starting point for interpreting all subsequent nanoscale transformations in the following scan.

2.2 | Dynamic Electrochemical Processes During the Second CV Scan

The following observations correspond to the second CV scan. The Cu nanoparticles remaining on the GC surface after the first CV cycle (Figure 2e) are crucial, as they act as preferential sites for further nucleation and growth [11]. With these initial conditions established, we examine how the electrode potential and the current relate to the dynamic local changes observed at the nanoscale.

2.2.1 | *Global Electrochemical Dynamics*

In situ TEM observations provide a detailed view of the dynamic evolution of the electrode surface during the voltammetric scan, capturing both general trends and particle-specific behaviors. It is important to note that while the CV trace represents the integrated electrochemical response of the entire electrode, the TEM viewing area captures only a small fraction of the total electrode surface. Furthermore, a reliable interpretation of in situ

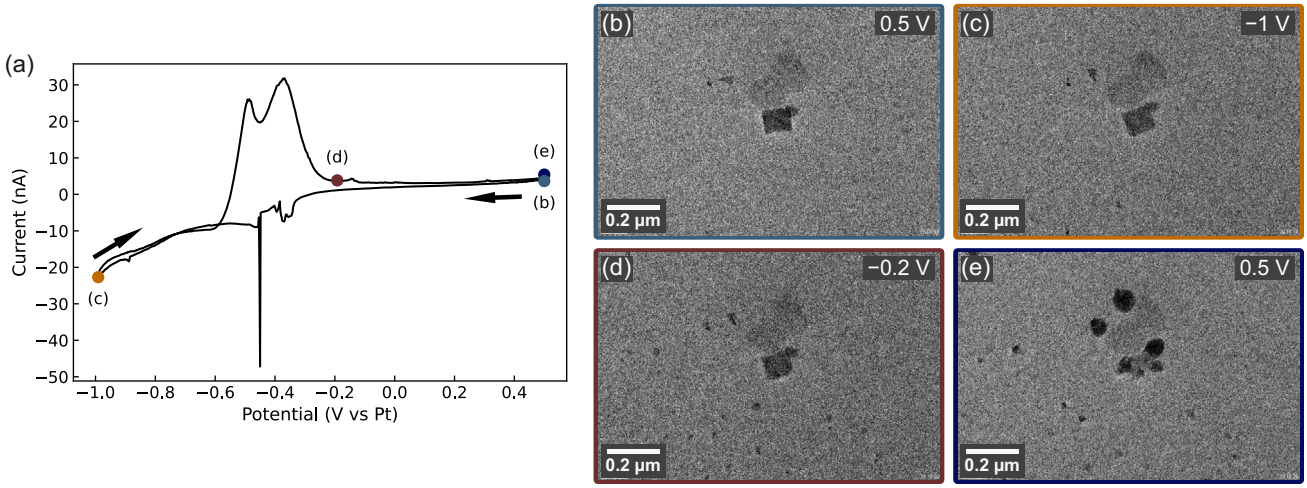

FIGURE 2 | Electrochemical response and corresponding in situ TEM observations during the first CV scan. (a) CV curve of the first scan, recorded between +0.5 and −1.0 V at a scan rate of 100 mV/s. The arrows indicate the scan direction. (b–e) In situ TEM images of the electrode surface at: (b) +0.5 V (initial potential), (c) −1 V, (d) −0.2 V, and (e) +0.5 V (final potential).

EC-TEM must account for coupled experimental factors such as electron-beam-induced radiolysis and transport limitations inherent to the confined liquid environment [59].

Despite these spatial and mechanistic limitations, correlating the overall current profile with the evolution of the total projected particle area (calculations described in the Supporting Information, Section S4) provides valuable insight into the dynamics of electrochemical nucleation, growth, and dissolution. Crucially, this dual analysis allows us to track local processes such as particle growth, dissolution, and coalescence that collectively shape the global electrochemical response [11, 29].

As shown in Figure 3a, the particle area follows the overall electrochemical evolution of the system, while the representative TEM snapshots and schematic illustration in Figure 3b–e summarize the dominant morphological regimes observed during the experiment. Importantly, the labeled particles (P1–P6) highlighted in Figure 3a,c–e are discussed individually in the following sections.

As shown in Figure 3 and Video S2, the cathodic sweep initiates growth on the residual Cu particles while simultaneously triggering the nucleation of new particles across the electrode surface. Upon reaching the first cathodic peak (Figure 3a), these particles undergo radial growth (Figure 3b,c), expanding uniformly as more copper is deposited.

As the potential becomes more negative, a second cathodic peak appears, coinciding with a morphological transition in several particles. At this point, dendritic growth becomes apparent (Figure 3b,c), characteristic of metal growth under a mass transport-limited regime aggravated by high overpotential [64]. This transition is enhanced by the confined electrolyte beneath the O_2 bubble. Within this confined volume, local Cu^{2+} depletion develops rapidly at active growth sites. As noted by Merkens et al. [55], the chip design inherently limits the flow velocity in the imaging area. Bubble formation further decreases the effective electrolyte thickness and increases flow resistance, generating a confined liquid layer with a limited Cu^{2+} reservoir in which mass transport is governed by slow diffusion. Although the electrode is not fully isolated from the bulk electrolyte, these restricted transport conditions promote rapid local depletion during cathodic polarization, leading to localized mass-transport limitations that trigger the observed dendritic growth.

In the anodic region, the dominant particle behavior shifts toward dissolution (Figure 3b,e). Dissolution initially proceeds slowly, but becomes significantly more pronounced as the potential reaches

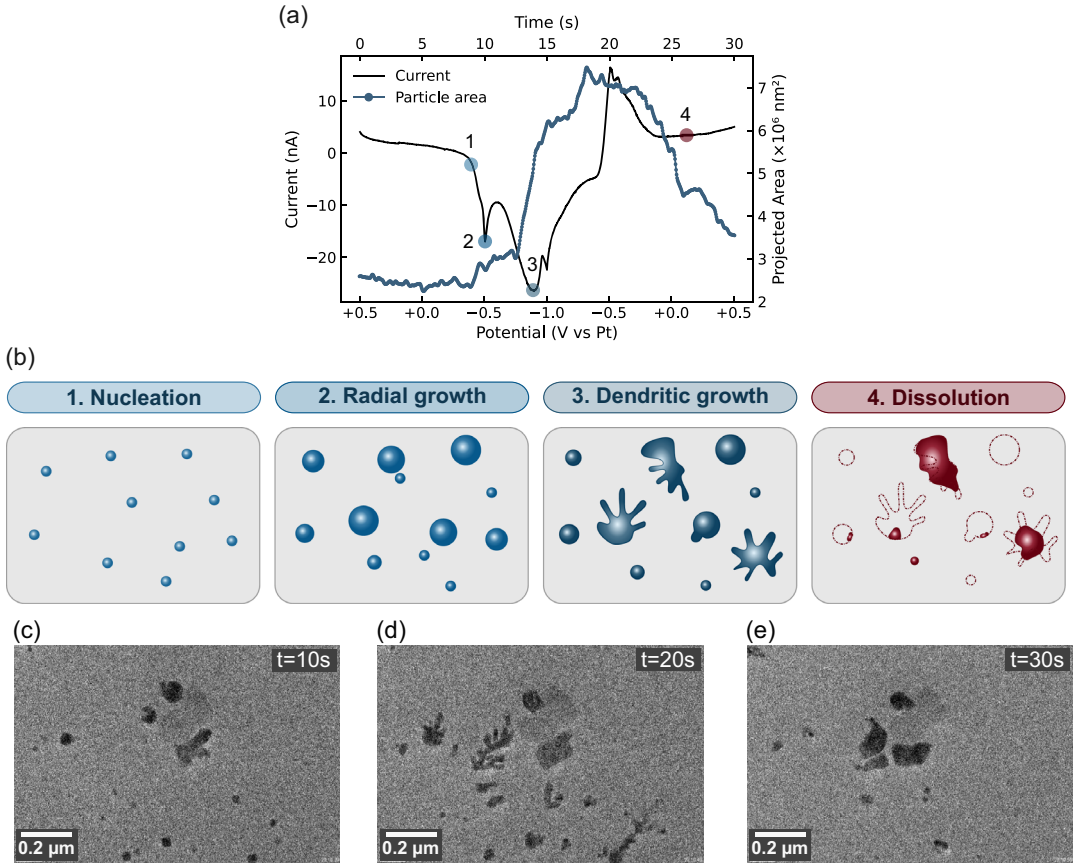

FIGURE 3 | Correlated global electrochemical response and localized nanoparticle evolution. (a) Current (black line) and total projected particle area (blue) as a function of time and potential during the second scan. The projected area corresponds to the summed contribution of all tracked particles within the TEM observation window. (b) Simplified schematic representation of the dominant morphological regimes observed during the experiment, including nucleation, radial and dendritic growth, and dissolution. (c–e) Representative in situ EC-TEM images acquired during the second CV scan (Video S2) showing the evolution of the nanoparticle population at different stages of the electrochemical process: (c) 10 s, (d) 20 s, and (e) 30 s. Arrows identify particles P1–P6 discussed later in the manuscript.

−0.25 V (following the anodic peak), leading to a decrease in particle size and, in some cases, complete disappearance. However, certain particles deviate from this overall trend and exhibit localized non-classical pathways. These unique phenomena are analyzed and discussed in detail in the following sections.

2.2.2 | *Non-classical Growth*

In situ observations allow us to distinguish between different growth mechanisms at the nanoscale. We observe classical pathways, characterized by the direct attachment of ions at the particle/electrolyte interface, leading to initial isotropic, radial growth. However, beyond these classical routes, in situ EC-TEM reveals discrete, particle-level events, such as surface migration, ripening interactions, aggregation, and coalescence, likely driven by local concentration gradients and confinement effects. These processes are tracked through real-time measurements of particle position, projected area, and perimeter evolution of individual particles in real time (Figures 4–6).

2.2.2.1 | Proximity-Driven Ripening Electrochemical Ostwald Ripening. Our in situ EC-TEM observations reveal a non-classical event involving two neighboring particles, P1 and P2 (Figure 4 and Video S3). Initially separated by approximately 53 nm (center-to-center distance), these particles undergo a proximity-dependent, ripening-like interaction consistent with an electrochemical Ostwald ripening process, accompanied by progressive particle relocation and mass redistribution. Quantitative evidence of this process is obtained from the time-resolved evolution of their projected areas (Figure 4b) and from the corresponding regression analysis of the area-change rates (Section S6, Supporting Information).

During the early interaction stage (8.3–10.64 s), the correlation between the shrinking of P1 and the growth of P2 yields a Pearson coefficient of $r = -0.48$ ($p = 1.41 \times 10^{-4}$), indicating an inverse but still moderately scattered relationship between both particles. As the particles approach one another, the interaction intensifies. At 10.26 s, when the center-to-center separation decreases to approximately 30 nm (Figure 4d), P2 undergoes a sudden relocation event toward P1 with a velocity of 0.61 μm s^{-1} (Figure S4a). This displacement marks the kinetic transition into a strongly coupled interaction regime.

Within the subsequent 0.38 s interval (10.26–10.64 s) (Figure 4b insert, Figure 4e,f), the correlation between both particles reaches a Pearson coefficient of $r = -0.99$ ($p = 1.97 \times 10^{-7}$). The calculated transfer slope during this interval is −1.22, whereas a theoretical slope of −1.0 corresponds to a perfectly closed one-to-one mass exchange. Our result indicates that P2 captures mass from two simultaneous sources: the local mass transfer from P1 and the continued Cu electrodeposition from the electrolyte. This process culminates with the disappearance of P1 near the TEM resolution limit as it consolidates with P2 into Particle 3 (P3) (Figure 4e,f).

Due to the inherent spatial and temporal resolution limitations of in situ EC-TEM, we cannot definitively rule out whether P1 fully dissolved through an electrochemical ripening process or whether a final aggregation event also occurred. Nevertheless, the inverse relationship observed just before disappearance strongly supports an electrochemical Ostwald ripening mechanism, in which atoms that detach from a less stable particle are incorporated into a neighboring, more stable, or more rapidly growing particle [19, 65].

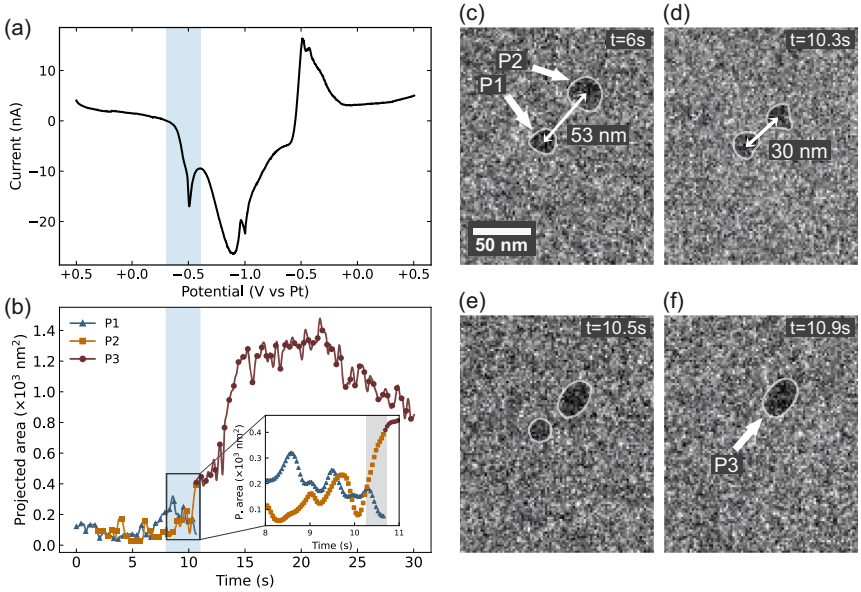

FIGURE 4 | Dynamic evolution of nanoparticles undergoing Ostwald ripening. (a) Current response during the second cyclic voltammetry scan with the interaction regime between P1 and P2 highlighted (blue region). (b) Evolution of projected areas of Particles P1 (▲), P2 (■), and P3 (●) during the second CV scan versus time. A zoomed inset highlights the ripening interval for P1 and P2 for the range 8–11 s, with the range from 10.26 to 10.64 s highlighted. (c–f) Representative in situ EC-TEM images (Video S3) showing the dynamic interaction between P1 and P2: (c) initial configuration at $t = 6$ s with a center-to-center separation of 53 nm, (d) reduced separation (~30 nm) immediately before interaction at $t = 10.3$ s, (e) intermediate stage during the mass-transfer/coalescence process at $t = 10.5$ s, and (f) formation of the resulting particle P3 at $t = 10.9$ s. White arrows identify the tracked particles discussed in the text, and particle outlines are lightly highlighted to aid visualization.

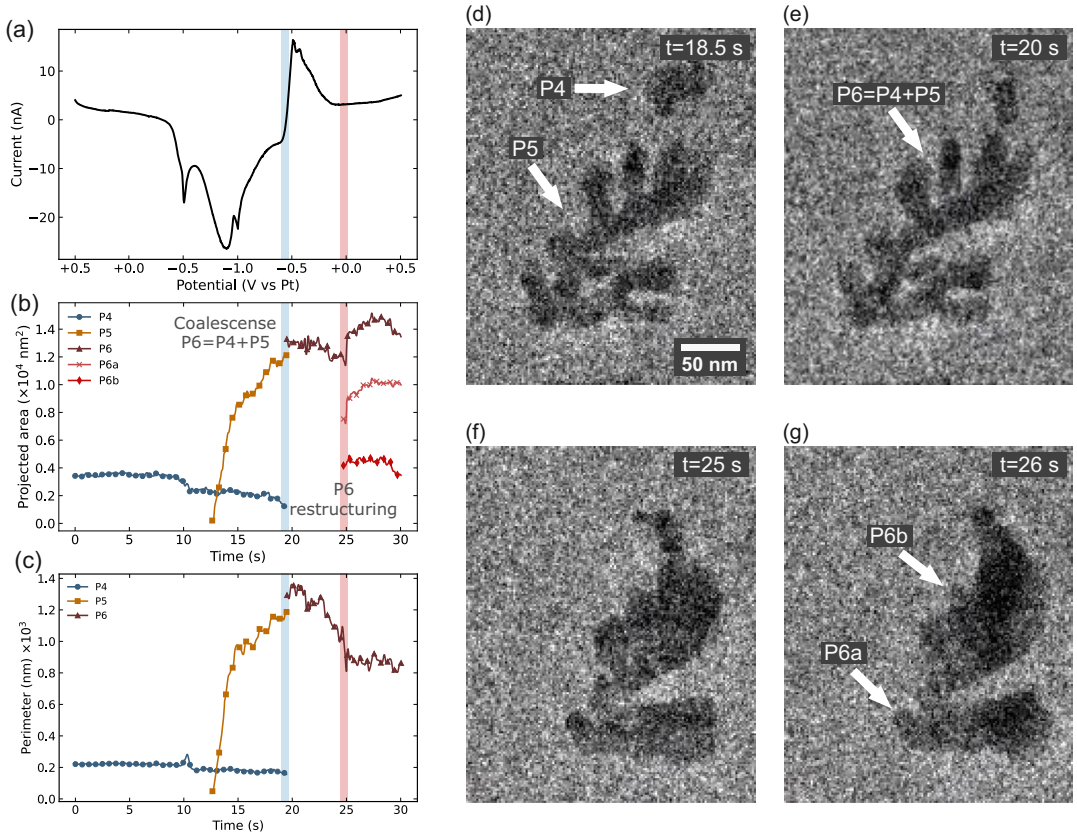

FIGURE 5 | Particle-resolved evolution of dendritic growth, coalescence, and anodic restructuring during the second CV scan. (a) Current response during the second cyclic voltammetry scan, with the coalescence and restructuring intervals highlighted in blue and red, respectively. (b) Projected area evolution of Particles 4 (●), 5 (■), 6 (▲), 6a (×), 6b (♦), as a function of time. After particle division, the projected area assigned to P6 corresponds to the combined projected areas of P6a and P6b. (c) Projected perimeter evolution of the same particles during the second CV scan. (d–f) Representative in situ EC-TEM images showing the morphological evolution of the particles: (d) 18.5 s, (e) 20 s, (f) 25 s, and (g) 26 s.

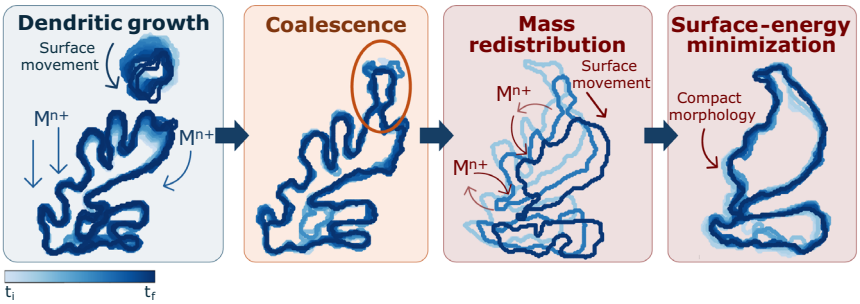

FIGURE 6 | Conceptual schematic of dendritic growth, coalescence, and anodic restructuring pathways observed during the electrochemical experiment. The schematic illustrates the proposed sequence of dendritic growth, coalescence, and anodic restructuring observed during the second CV scan.

Beyond mass redistribution, this interaction also modifies surface dynamics. Analysis of particle trajectories via mean squared displacement (MSD) (Section S7, Supporting Information) reveals a contrast in mobility between particles. Importantly, the diffusion coefficients extracted from this analysis should not be interpreted as the thermal surface diffusion of adatoms. Instead, they quantify an effective centroid mobility. We note that this description is phenomenological, as the present data do not resolve the underlying atomistic rearrangement pathways. The observed mobility is attributed to coupled electrochemical and interfacial processes operating within the confined environment, including local mass redistribution and field-driven effects.

To compare relative mobilities, we define an apparent diffusion coefficient (D_{app}) extracted from the short-time MSD regime, where motion is least affected by long-range confinement or directional relocation effects (Section S7.2, Supporting Information).

The precursors, P1 and P2, exhibit a local nondirectional displacement at small time intervals ($\alpha \approx 0.95$), and relatively small apparent diffusion coefficients ($D_{app} \approx 4.5 \times 10^{-6}$ and 3.4×10^{-5} $\mu m^2\ s^{-1}$, respectively). At larger lag times, both particles transition toward strongly subdiffusive behavior ($\alpha = 0.27$ and 0.31), indicating confinement within localized surface regions (Figure S4b). This transition indicates that while the

particles undergo a stochastic "random walk" at the nanoscale, they are restricted to a specific area.

In contrast, P3 displays a substantial increase in mobility ($D_{app} \approx 1.9 \times 10^{-3}$ μm^2 s^{-1}). Its MSD evolves from a diffusive motion ($\alpha = 1.08$) toward a directed, ballistic-like regime ($\alpha = 1.95$ at larger time lags). This transition is consistent with the rapid relocation events observed in the position versus time plot (Figure S4a), where P3 reaches velocities up to 0.53 μm s^{-1}. At large lag times, however, the statistical reliability of the MSD decreases due to the progressively smaller number of independent displacement pairs contributing to the calculation.

Overall, these observations underscore that localized ripening interactions can act as a kinetic trigger that transform confined precursors into highly mobile entities, and underscore the highly localized and dynamic nature of electrochemical processes at the nanoscale. Crucially, these substantial mass-redistribution events do not produce a detectable change in the global electrochemical current.

2.2.2.2 | Dendritic Growth and Coalescence. The interaction between Particles 4 (P4) and 5 (P5) offers a complex example of how morphological transitions modulate local mass transfer and mobility (Figure 5, Video S4). Unlike the previous case, P4 is present from the beginning of the scan and exhibits a relatively stable projected area (Figure 5a,b). The dynamics shift at $t = 10$ s, coinciding with the first cathodic peak. At this point, P4 experiences a decrease in projected area, followed by a period of slower, steady shrinkage until 19 s. Simultaneously, this electrochemical landmark acts as a kinetic trigger for lateral particle mobility on the GC surface, with P4 exhibiting lateral mobility ($D_{app} \approx 2.2 \times 10^{-5}$ μm^2 s^{-1}) (Section S7.4, Supporting Information).

At approximately 13 s, P5 nucleates and immediately develops a dendritic morphology characterized by elongated, high-curvature branches extending toward the neighboring P4 (Figure 5b,d). As cathodic polarization proceeds, the motion of P4 evolves from relatively stochastic displacement toward a more directional approach toward P5 (Figure S5a). This transition becomes particularly apparent near $t = 17$ s, when both particles approach one another while P4 continues to lose projected area.

The coupled perimeter and projected-area evolution as shown in Figure 5b,c suggests that this interaction is accompanied by localized mass redistribution. In particular, the pronounced perimeter increase observed for P5 during cathodic polarization reflects the rapid development of dendritic, high-curvature features. These unstable regions likely promote enhanced local ion fluxes and preferential incorporation of dissolved Cu species originating from the neighboring particle. Consequently, as P4 approaches the dendritic front of P5, its projected area progressively decreases while P5 continues to grow and branch.

This interaction culminates at approximately 19 s, immediately before the onset of the anodic peak, when P4 and P5 undergo physical coalescence to form Particle 6 (P6) (Figures 5e and 6). This sequence underscores how local gradients in a confined environment can force the consolidation of nearby particles during electrochemical growth, thereby establishing the highly ramified morphologies that subsequently undergo anodic restructuring in the anodic regime.

2.2.3 | Anodic Surface-Energy-Driven Restructuring and Division

As the scan reverses toward anodic potentials, the system transitions from a regime of mass accumulation to one of morphological stabilization. Between 20 and 25 s, P6 undergoes a pronounced morphological reorganization (Figures 5f and 6). During this interval, the particle perimeter decreases sharply while the total projected area remains comparatively stable (Figure 5b,c). This pronounced decoupling between perimeter and projected area indicates a transition from highly ramified dendritic structures toward more compact morphologies. While the observed evolution is consistent with a tendency toward surface-energy minimization, our data provide only a phenomenological description based on geometric evolution and do not allow us to uniquely resolve the underlying microscopic mechanisms driving this process.

This morphological reorganization is particularly pronounced at the dendritic tips and high-curvature regions formed during the cathodic phase. These high-energy regions likely undergo preferential dissolution, followed by local redeposition and/or surface diffusion toward more stable sites. During this restructuring stage, P6 also exhibits slight lateral displacement along the GC surface (Figure 6 and Video S4), suggesting a transient reduction in interfacial pinning as the dendritic morphology reorganizes. As restructuring progresses, the elongated dendritic morphology collapses into a more compact configuration, ultimately leading to the division of P6 into two daughter particles (P6a and P6b) at approximately 25 s (Figures 5b,c,g and 6).

Interestingly, the combined projected area of the daughter particles (1.4×10^4 nm^2) appears slightly larger than that of the precursor P6 before division (1.2×10^4 nm^2). This apparent increase is attributed to morphological flattening and loss of ramified dendritic structures, which increase the projected footprint of the particles as they evolve toward more compact and thermodynamically favorable geometries.

We interpret this restructuring as being consistent with two coupled processes that qualitatively account for the observed morphology changes: (i) coupled dissolution and local redeposition/adsorption, where the oxidation of high-energy dendritic features generates a transient local concentration of Cu species that subsequently redeposit into nearby stable regions, thereby redistributing mass without substantial loss to the bulk electrolyte and (ii) potential-induced surface diffusion, where the anodic bias enhances surface adatom mobility [21], allowing atoms to migrate from unstable high-curvature regions toward energetically more favorable sites without fully entering solution.

During the postrestructuring phase (25–30 s), the perimeter stabilizes, indicating that the particle has adopted a more compact and energetically favorable shape. These pathways, consistent with a thermodynamic tendency toward reduced surface energy, manifested through the elimination of high-curvature features, contribute substantially to the final morphology of the deposit but remain invisible in the voltammetric profile. This highlights the essential value of nanoscale, time-resolved EC-TEM in resolving dynamic phenomena that cannot be inferred from macroscopic signals

2.3 | Implications for Electrochemical Phase Transformations: From Classical to Non-classical Pathways

Our combined electrochemical and TEM measurements reveal that relying on the voltammetric profile (or *I*–*t* curves) obscures the discrete processes that define the earliest stages of electrochemical phase transformations, i.e., electrochemical nucleation, growth, and dissolution. Although the voltammetric profile reflects the global behavior of the interface, it can mask the wide variety of surface processes at play at the local level, since very different mechanisms such as ripening-like interactions, coalescence, surface diffusion, and restructuring leave little or no distinct signature in the integrated global current.

Classical interpretations and global current–deposit correlations assume uniform, atom-by-atom growth and smooth dissolution. However, our data show that particle–particle interactions, lateral movement, and surface-energy-driven restructuring can reshape the deposit long before stable structures form, as anticipated by a series of recent works that employed ex situ high-resolution TEM characterization [19, 21–24, 44, 66], in situ optical microscopy [32, 33, 35], or scanning-probe methods [18, 29].

For instance, coalescence redistributes mass and offers an alternative growth pathway, yet it involves essentially no net charge transfer across the interface. Likewise, ripening-like interactions redistribute mass between neighboring particles without producing a pronounced signature in the global current response. In parallel, anodic restructuring pathways involving preferential dissolution of high-curvature regions, local redeposition, and surface diffusion progressively transform dendritic structures into more compact morphologies.

The potential cycling and confined thin electrolyte layer of the EC-TEM cell create strong nonequilibrium local conditions in which particles evolve not only through direct electrochemical growth and dissolution, but also through structural reorganization pathways driven by local concentration gradients, confinement effects, and thermodynamic tendencies toward reduced surface energy. These alternative pathways are not captured by conventional classical analyses. Although the global contribution of these events remains difficult to quantify, their influence on the early-stage morphology and spatial evolution of the deposit appears substantial.

Recognizing that such non-classical pathways can proceed largely "silently" within an electrochemical curve (CV or CA), we capture this behavior by pairing global electrochemical measurements with real-time particle-resolved imaging and phenomenological analysis to resolve the early-stage dynamics of electrochemical phase transformations.

3 | Conclusions

Our in situ EC-TEM investigation provides unprecedented insights into the dynamic evolution of Cu nanoparticles during electrochemical growth and dissolution. Through direct, real-time observation and quantification, we have unveiled a rich landscape of non-classical phenomena that challenge simplified views of electrochemical growth and dissolution, demonstrating that nanoparticles are highly dynamic entities on the electrode surface. Although the underlying mechanisms governing these complex behaviors are multifaceted, the ability to directly visualize and quantify these events as they happen offers a crucial foundation for future research.

While the global CV captures the onset of electron transfer, only particle-resolved imaging can distinguish classical atom-by-atom growth and dissolution processes, and non-classical pathways involving collective particle motion, restructuring, and mass redistribution. These local events often decouple from the global current, demonstrating that one cannot anticipate the underlying particle dynamics from electrochemical data alone.

Specifically, our work highlights two critical aspects:

1. Direct particle–particle interactions and mass transfer, exemplified by the quantitative analysis of ripening and aggregation events during cathodic polarization.
2. Dynamic restructuring and particle splitting during anodic processes, where particles undergo notable morphological changes driven by surface-energy-minimization and, remarkably, can split into smaller entities.

Together, these observations demonstrate the importance of combining global electrochemical measurements with real-time nanoscale imaging to identify and evaluate the contribution of non-classical pathways during electrochemical phase transformations.

These findings offer a more complete picture of nanoparticle behavior under electrochemical bias. By direct visualization of processes like particle surface movement, coalescence, restructuring, and division, this study provides insights into the kinetics of electrochemical growth and dissolution, crucial for advancing the understanding of nanomaterials. Thus, these localized non-classical processes proceed "silently" within the global electrochemical signal yet decisively dictate the spatial distribution and morphology of the final deposit. While further investigation is needed to fully uncover all underlying mechanisms and implications, this framework is vital for the design and optimization of electrochemical systems, where phenomena such as corrosion, electrocatalysis, and alloy deposition likely involve similarly intricate local dynamics.

4 | Experimental Section/Methods

4.1 | Materials and Chemicals

Copper (II) sulfate pentahydrate (CuSO4·5H2O, ≥99%, Sigma Aldrich) and sulfuric acid (H2SO4, 96%, Carlo Erba Reagents) were used as received. All aqueous solutions were prepared using ultrapure water (18.2 MΩ·cm, Milli-Q system). Prior to each experiment, the electrolyte was sonicated for 20 min to ensure degassing.

4.2 | In Situ Liquid-Cell TEM Setup

In situ electrochemical experiments were performed using a Poseidon Select liquid-cell TEM holder (Protochips, Morrisville, NC). The setup featured a miniaturized three-electrode cell integrated within the liquid-cell assembly, controlled by a Gamry Reference 620 potentiostat (Gamry Instruments Inc., Warminster, PA). Electrolyte flow was maintained at 120 $\mu L\,h^{-1}$ using a Harvard 11 Elite syringe pump (Harvard Apparatus Inc., Holliston, MA).

The electrochemical liquid-cell consists of two silicon chips with electron-transparent silicon nitride (SiN_x) windows (50 nm thick), hermetically sealed within the holder. The electrochemical chip (ec-chip) integrates a coplanar three-electrode configuration. This setup includes platinum counter (CE) and pseudoreference (RE) electrodes, and a GC working electrode (WE) deposited directly over the electron-transparent window. A 500 nm spacer (SU-8) defines the thickness of the liquid layer.

- Flow dynamics: While the inlet flow is 120 $\mu L\,h^{-1}$, fluidic simulations estimate the effective linear flow velocity in the imaging area to be lower than $6 \times 10^{-6}\,m\,s^{-1}$ due to the microfluidic design and the inherent fluidic resistance of the narrow channels [56].
- Resolution enhancement (bubble formation): To mitigate the window bulging caused by the TEM vacuum, which increases the liquid layer thickness and lowers resolution, an oxidative potential of 0.8 V was applied to generate a confined O_2 gas bubble over the WE. This bubble displaces the bulk electrolyte, creating an ultra-thin liquid layer (50 nm) [55]. This procedure significantly enhanced image contrast, enabling the detection and tracking of nanoparticles as small as 10 nm (Figure S2).

4.2.1 | TEM Imaging

In situ microscopy was performed using a JEM-2100 TEM (JEOL, Tokyo, Japan) operated at 200 keV in bright-field mode. The electron flux was calibrated to 3128.34 $e\,nm^{-2}\,s^{-1}$ (dose rate of 1.38×10^8 Gy s^{-1}) to minimize radiolysis artifacts.

4.3 | In Situ Deposition Protocol

Following the establishment of the high-resolution imaging regime, the following experiments were conducted:

1. Surface cleaning: CA at +0.5 V for 60 s. This step was critical to dissolve most of the pre-existing copper particles, nuclei, or adatoms, ensuring that the subsequent deposition started from the cleanest GC surface.
2. Voltammetric deposition: The deposition process was captured during a CV performed between +0.5 to −1 V versus Pt at a scan rate of 100 mV s^{-1}.

Note on analysis: Although multiple cycles were recorded, the quantitative analysis of nanoparticle nucleation, growth, and the phenomenon presented in the manuscript focuses on the first two scans, specifically the second scan.

Acknowledgments

M. P. gratefully acknowledges the financial support provided by the Research Foundation – Flanders (FWO) through the fundamental research project G0C3121N. The authors affiliated with the Jožef Stefan Institute (JSI) acknowledge the ARIS (Slovenian Research Agency) for financial support under Program P2-0084 and projects N1-0196, J7-4636-1, J2-4433-2, and GC-0004 (Chronostore). S. S. P. acknowledges support from the ARIS project Z2-50057. L. J. S. S. acknowledges the suport from the ARIS project PR-12334 (Young Researcher Program). D. T. acknowledges financial support from the Fonds de la Recherche dans l'Industrie et l'Agriculture (FRIA). J. U. acknowledges financial support from the Fédération Wallonie-Bruxelles through the ARC-Consolidator grant RENEGADE. D. T. and A. L. acknowledge funding from Innoviris through the R&D project NDIAMO. AI tools (ChatGPT and Google Gemini) were used for code assistance and text editing. All computational procedures, analyses, and figures were validated by the authors.

Funding

This study was supported by FWO (Grant G0C3121N), ARIS (Slovenian Research Agency) (Grant N1-0196, J7-4636-1, J2-4433-2, GC-0004, PR-12334, P2-0084, and Z2-50057), Fédération Wallonie-Bruxelles through the ARC-Consolidator (Grant RENEGADE), Innoviris (Grant NDIAMO).

Conflicts of Interest

The authors declare no conflicts of interest.

Data Availability Statement

The data that support the findings of this study are available from the corresponding author upon reasonable request.

References

1. D. J. Lockwood, K. Kondo, R. N. Akolkar, D. P. Barkey, and M. Yokoi, *Copper Electrodeposition for Nanofabrication of Electronics Devices* (Springer New York, 2014), https://doi.org/10.1007/978-1-4614-9176-7.

2. M. Paunovic and M. Schlesinger, *Fundamentals of Electrochemical Deposition* (John Wiley & Sons, Ltd., 2006), https://doi.org/10.1002/0470009403.

3. L. Zhao, Y. Wang, S. Jin, et al., "Rational Electrochemical Design of Hierarchical Microarchitectures for SERS Sensing Applications," *Nature Synthesis* 3 (2024): 867–877, https://doi.org/10.1038/s44160-024-00553-1.

4. Y. Liu, H. You, Y. C. Kimmel, D. V. Esposito, J. G. Chen, and T. P. Moffat, "Self-Terminating Electrodeposition of Pt on WC Electrocatalysts," *Applied Surface Science* 504 (2020): 144472, https://doi.org/10.1016/j.apsusc.2019.144472.

5. Z. Zhang, C. Feng, C. Liu, et al., "Electrochemical Deposition as a Universal Route for Fabricating Single-Atom Catalysts," *Nature Communications* 11 (2020): 1215, https://doi.org/10.1038/s41467-020-14917-6.

6. E. Plaza-Mayoral, K. N. Dalby, H. Falsig, I. Chorkendorff, P. Sebastián-Pascual, and M. Escudero-Escribano, "Preparation of Tunable Cu–Ag Nanostructures by Electrodeposition in a Deep Eutectic Solvent," *ChemElectroChem* 11 (2024): e202400094, https://doi.org/10.1002/celc.202400094.

7. M. Bernal Lopez and J. Ustarroz, "Electrodeposition of Nanostructured Catalysts for Electrochemical Energy Conversion: Current Trends and Innovative Strategies," *Current Opinion in Electrochemistry* 27 (2021): 100688, https://doi.org/10.1016/j.coelec.2021.100688.

8. S. A. Lee, J. W. Yang, S. Choi, and H. W. Jang, "Nanoscale Electrodeposition: Dimension Control and 3D Conformality," *Exploration* 1 (2021): 20210012, https://doi.org/10.1002/EXP.20210012.

9. A. Milchev, *Electrocrystallization Fundamentals of Nucleation and Growth* (Kluwer Academic Publishers, 2002), https://doi.org/10.1007/b113784.

10. M. E. Palomar-Pardavé and T. Le Manh, *Nucleation and Growth in Applied Materials* (Elsevier, 2024), https://doi.org/10.1016/C2021-0-02052-6.

11. D. Torres, M. Bernal, A. Demaude, et al., "Distribution of Copper Electrochemical Nucleation Activities on Glassy Carbon: A New Perspective Based on Local Electrochemistry," *Journal of the Electrochemical Society* 169 (2022): 102513, https://doi.org/10.1149/1945-7111/ac9717.

12. J. Ustarroz, "Current Atomic-Level Understanding of Electrochemical Nucleation and Growth on Low-Energy Surfaces," *Current Opinion in Electrochemistry* 19 (2020): 144–152, https://doi.org/10.1016/j.coelec.2019.12.001.

13. B. R. Scharifker and J. Mostany, *Developments in Electrochemistry* eds. D. Pletcher, Z.-Q. Tian, D E. Williams, (John Wiley & Sons, 2014), 65–75, https://doi.org/10.1002/9781118694404.ch4.

14. A. Milchev, "Electrochemical Phase Formation: Classical and Atomistic Theoretical Models," *Nanoscale* 8 (2016): 13867–13872, https://doi.org/10.1039/c6nr02354a.

15. A. Radisic, P. M. Vereecken, J. B. Hannon, P. C. Searson, and F. M. Ross, "Quantifying Electrochemical Nucleation and Growth of Nanoscale Clusters Using Real-Time Kinetic Data," *Nano Letters* 6 (2006): 238–242, https://doi.org/10.1021/nl052175i.

16. M. H. Nielsen, D. Li, H. Zhang, et al., "Investigating Processes of Nanocrystal Formation and Transformation via Liquid Cell TEM," *Microscopy and Microanalysis* 20 (2014): 425–436, https://doi.org/10.1017/S1431927614000294.

17. J. Yang, C. M. Andrei, Y. Chan, et al., "Liquid Cell Transmission Electron Microscopy Sheds Light on the Mechanism of Palladium Electrodeposition," *Langmuir: The ACS Journal of Surfaces and Colloids* 35 (2019): 862–869, https://doi.org/10.1021/acs.langmuir.8b02846.

18. R. L. Harniman, D. Plana, G. H. Carter, K. A. Bradley, M. J. Miles, and D. J. Fermín, "Real-Time Tracking of Metal Nucleation via Local Perturbation of Hydration Layers," *Nature Communications* 8 (2017): 971, https://doi.org/10.1038/s41467-017-01087-1.

19. H. E. M. Hussein, R. J. Maurer, H. Amari, et al., "Tracking Metal Electrodeposition Dynamics from Nucleation and Growth of a Single Atom to a Crystalline Nanoparticle," *ACS Nano* 12 (2018): 7388–7396, https://doi.org/10.1021/acsnano.8b04089.

20. V. Tsakova, "Theory of Electrochemical Nucleation and Growth-Revisited?," *Journal of Solid State Electrochemistry* 24 (2020): 2183–2185, https://doi.org/10.1007/s10008-020-04676-1.

21. J. Ustarroz, J. A. Hammons, T. Altantzis, A. Hubin, S. Bals, and H. Terryn, "A Generalized Electrochemical Aggregative Growth Mechanism," *Journal of the American Chemical Society* 135 (2013): 11550–11561, https://doi.org/10.1021/ja402598k.

22. J. Ustarroz, T. Altantzis, J. A. Hammons, A. Hubin, S. Bals, and H. Terryn, "The Role of Nanocluster Aggregation, Coalescence, and Recrystallization in the Electrochemical Deposition of Platinum Nanostructures," *Chemistry of Materials* 26 (2014): 2396–2406, https://doi.org/10.1021/cm403178b.

23. J. Ustarroz, X. Ke, A. Hubin, S. Bals, and H. Terryn, "New Insights Into the Early Stages of Nanoparticle Electrodeposition," *The Journal of Physical Chemistry C* 116 (2012): 2322–2329, https://doi.org/10.1021/jp210276z.

24. S. C. S. Lai, R. A. Lazenby, P. M. Kirkman, and P. R. Unwin, "Nucleation, Aggregative Growth and Detachment of Metal Nanoparticles During Electrodeposition at Electrode Surfaces," *Chemical Science* 6 (2015): 1126–1138, https://doi.org/10.1039/c4sc02792b.

25. J. Kim, D. Kang, S. Kang, B. H. Kim, and J. Park, "Coalescence Dynamics of Platinum Group Metal Nanoparticles Revealed by Liquid-Phase Transmission Electron Microscopy," *iScience* 25 (2022): 104699, https://doi.org/10.1016/j.isci.2022.104699.

26. S. Karthika, T. K. Radhakrishnan, and P. Kalaichelvi, "A Review of Classical and Nonclassical Nucleation Theories," *Crystal Growth & Design* 16 (2016): 6663–6681, https://doi.org/10.1021/acs.cgd.6b00794.

27. P. Zhao, D. Houghton, J. J. Tully, et al., "Optical and Electron Transparent Polycrystalline Boron Doped Diamond Membranes for Nanoscale Correlative Structure-Electrochemical Measurements," *ACS Nano* 19 (2025): 41637–41647, https://doi.org/10.1021/acsnano.5c13873.

28. D. Torres, *PhD Thesis, Insights into Electrochemical Nucleation & Growth: New Perspective from Local Electrochemistry* (Universite Libre de Bruxelles, 2025).

29. D. Torres, M. Bernal, and J. Ustarroz, "Deciphering Spatially-Resolved Electrochemical Nucleation and Growth Kinetics by Correlative Multimicroscopy," *Small Methods* 9 (2025): 2401029, https://doi.org/10.1002/smtd.202401029.

30. D. Torres, J. Bailly, M. Bernal, L. B. Coelho, and J. Ustarroz, "Electrochemical Nucleation and the Role of the Surface State: Unraveling Activity Distributions with a Cross-System Examination and a Local Electrochemistry Approach," *Journal of Solid State Electrochemistry* 28 (2024): 1719–1734, https://doi.org/10.1007/s10008-023-05760-y.

31. M. Bernal, D. Torres, S. S. Parapari, et al., "A Microscopic View on the Electrochemical Deposition and Dissolution of Au with Scanning Electrochemical Cell Microscopy – Part I," *Electrochimica Acta* 445 (2023): 142023, https://doi.org/10.1016/j.electacta.2023.142023.

32. P. Ciocci, D. Valavanis, G. N. Meloni, J. Lemineur, P. R. Unwin, and F. Kanoufi, "Optical Super-Localisation of Single Nanoparticle Nucleation and Growth in Nanodroplets," *ChemElectroChem* 10 (2023): e202201162, https://doi.org/10.1002/celc.202201162.

33. J.-F. Lemineur, H. Wang, W. Wang, and F. Kanoufi, "Emerging Optical Microscopy Techniques for Electrochemistry," *Annual Review of Analytical Chemistry* 15 (2022): 57–82, https://doi.org/10.1146/annurev-anchem-061020-015943.

34. J. F. Lemineur, P. Ciocci, J. M. Noël, H. Ge, C. Combellas, and F. Kanoufi, "Imaging and Quantifying the Formation of Single Nanobubbles at Single Platinum Nanoparticles during the Hydrogen Evolution Reaction," *ACS Nano* 15 (2021): 2643–2653, https://doi.org/10.1021/acsnano.0c07674.

35. J. F. Lemineur, J. M. Noël, D. Ausserré, C. Combellas, and F. Kanoufi, "Combining Electrodeposition and Optical Microscopy for Probing Size-Dependent Single-Nanoparticle Electrochemistry," *Angewandte Chemie International Edition* 57 (2018): 11998–12002, https://doi.org/10.1002/anie.201807003.

36. F. M. Ross, *Liquid Cell Electron Microscopy* (Cambridge University Press, 2017), https://doi.org/10.1017/9781316337455.

37. M. Bernal, D. Torres, S. S. Parapari, et al., "A Microscopic View on the Electrochemical Deposition and Dissolution of Au with Scanning Electrochemical Cell Microscopy – Part II: Potentiostatic Dissolution and Correlation with In-Situ EC-TEM," *Electrochimica Acta* 492 (2024): 144302, https://doi.org/10.1016/j.electacta.2024.144302.

38. J. Yang, C. M. Andrei, G. A. Botton, and L. Soleymani, "In Liquid Observation and Quantification of Nucleation and Growth of Gold Nanostructures Using In Situ Transmission Electron Microscopy," *The Journal of Physical Chemistry C* 121 (2017): 7435–7441, https://doi.org/10.1021/acs.jpcc.6b10400.

39. M. Sun, H. G. Liao, K. Niu, and H. Zheng, "Structural and Morphological Evolution of Lead Dendrites During Electrochemical Migration," *Scientific Reports* 3 (2013): 3227, https://doi.org/10.1038/srep03227.

40. N. M. Schneider, J. H. Park, J. M. Grogan, D. A. Steingart, H. H. Bau, and F. M. Ross, "Nanoscale Evolution of Interface Morphology During Electrodeposition," *Nature Communications* 8 (2017): 2174, https://doi.org/10.1038/s41467-017-02364-9.

41. J. Park, S. Dutta, H. Sun, et al., "Toward Quantitative Electrodeposition via In Situ Liquid Phase Transmission Electron Microscopy: Studying Electroplated Zinc Using Basic Image Processing and 4D STEM," *Small Methods* 8 (2024): 2400081, https://doi.org/10.1002/smtd.202400081.

42. N. Ortiz Peña, D. Ihiawakrim, M. Han, et al., "Morphological and Structural Evolution of Co_3O_4 Nanoparticles Revealed by In Situ Electrochemical Transmission Electron Microscopy during Electrocatalytic Water Oxidation," *ACS Nano* 13 (2019): 11372–11381, https://doi.org/10.1021/acsnano.9b04745.

43. J. Dai, Y. Sun, Z. Liu, Y. Zhang, S. Duan, and R. Wang, "Using In Situ Transmission Electron Microscopy to Study Strong Metal-Support Interactions in Heterogeneous Catalysis," *Angewandte Chemie International Edition* 63 (2024): e202409673, https://doi.org/10.1002/anie.202409673.

44. H. Hu, R. Yang, and Z. Zeng, "Liquid-Phase TEM Study of Electrochemical Reactions at Multiple Interfaces," *Matter* 8 (2025): 101939, https://doi.org/10.1016/j.matt.2024.11.033.

45. Y. Yang, S. Louisia, S. Yu, et al., "Operando Studies Reveal Active Cu Nanograins for CO_2 Electroreduction," *Nature* 614 (2023): 262–269, https://doi.org/10.1038/s41586-022-05540-0.

46. J. Sung, Y. Bae, H. Park, et al., "Liquid-Phase Transmission Electron Microscopy for Reliable In Situ Imaging of Nanomaterials," *Annual Review of Chemical and Biomolecular Engineering* 13 (2022): 167–191, https://doi.org/10.1146/annurev-chembioeng-092120-034534.

47. Z. Guo, P. Paciok, R. Zandonella, et al., "Visualizing Electrochemical CO_2 Reduction Reaction: Recent Progress of In Situ Liquid Cell Transmission Electron Microscopy," *Advanced Functional Materials* 35 (2025): 2500915, https://doi.org/10.1002/adfm.202500915.

48. A. Radisic, F. M. Ross, and P. C. Searson, "In Situ Study of the Growth Kinetics of Individual Island Electrodeposition of Copper," *The Journal of Physical Chemistry B* 110 (2006): 7862–7868, https://doi.org/10.1021/jp057549a.

49. X. Zhang, W. Liu, Z. Chen, Y. Huang, W. Liu, and Y. Yu, "Pitfalls in Electrochemical Liquid Cell Transmission Electron Microscopy for Dendrite Observation," *Advanced Energy and Sustainability Research* 3 (2022): 2100160, https://doi.org/10.1002/aesr.202100160.

50. C. O'Regan, X. Zhu, J. Zhong, et al., "CTAB-Influenced Electrochemical Dissolution of Silver Dendrites," *Langmuir* 32 (2016): 3601–3607, https://doi.org/10.1021/acs.langmuir.6b00037.

51. J. Lee, D. Nicholls, N. D. Browning, and B. L. Mehdi, "Controlling Radiolysis Chemistry on the Nanoscale in Liquid Cell Scanning Transmission Electron Microscopy," *Physical Chemistry Chemical Physics* 23 (2021): 17766–17773, https://doi.org/10.1039/d0cp06369j.

52. B. Fritsch, S. Lee, A. Körner, N. M. Schneider, F. M. Ross, and A. Hutzler, "The Influence of Ionizing Radiation on Quantification for In Situ and Operando Liquid-Phase Electron Microscopy," *Advanced Materials* 37 (2025): 2415728, https://doi.org/10.1002/adma.202415728.

53. B. Fritsch, T. S. Zech, M. P. Bruns, et al., "Radiolysis-Driven Evolution of Gold Nanostructures – Model Verification by Scale Bridging In Situ Liquid-Phase Transmission Electron Microscopy and X-Ray Diffraction," *Advanced Science* 9 (2022): 2202803, https://doi.org/10.1002/advs.202202803.

54. N. Hodnik, G. Dehm, and K. J. J. Mayrhofer, "Importance and Challenges of Electrochemical In Situ Liquid Cell Electron Microscopy for Energy Conversion Research," *Accounts of Chemical Research* 49 (2016): 2015–2022, https://doi.org/10.1021/acs.accounts.6b00330.

55. Y. Yang, J. Feijóo, V. Briega-Martos, et al., "Operando Methods: A New Era of Electrochemistry," *Current Opinion in Electrochemistry* 42 (2023): 101403, https://doi.org/10.1016/j.coelec.2023.101403.

56. S. Merkens, G. De Salvo, J. Kruse, et al., "Quantification of Reagent Mixing in Liquid Flow Cells for Liquid Phase-TEM," *Ultramicroscopy* 245 (2023): 113654, https://doi.org/10.1016/j.ultramic.2022.113654.

57. P. Abellan, T. J. Woehl, L. R. Parent, N. D. Browning, J. E. Evans, and I. Arslan, "Factors Influencing Quantitative Liquid (Scanning) Transmission Electron Microscopy," *Chemical Communications* 50 (2014): 4873–4880, https://doi.org/10.1039/c3cc48479c.

58. S. Merkens, C. Tollan, G. De Salvo, et al., "Toward Sub-Second Solution Exchange Dynamics in Flow Reactors for Liquid-Phase Transmission Electron Microscopy," *Nature Communications* 15 (2024): 2522, https://doi.org/10.1038/s41467-024-46842-3.

59. M. El Marini, A. Leontev, A. Prasnikar, et al., "Electrochemical TEM: Simulating Electrochemistry Coupled with Radiolysis," *ACS Electrochemistry* 2 (2026): 336–352, https://doi.org/10.1021/acselectrochem.5c00396.

60. F. M. Ross, "Opportunities and Challenges in Liquid Cell Electron Microscopy," *Science* 350 (2015), https://doi.org/10.1126/science.aaa9886.

61. K. Bejtka, M. Fontana, C. I. Gho, et al., "Electrochemical Liquid Phase TEM in Aqueous Electrolytes for Energy Applications: The Role of Liquid Flow Configuration," *Small Methods* 9 (2025): 2401718, https://doi.org/10.1002/smtd.202401718.

62. R. Serra-Maia, P. Kumar, A. C. Meng, et al., "Nanoscale Chemical and Structural Analysis During In Situ Scanning/Transmission Electron Microscopy in Liquids," *ACS Nano* 15 (2021): 10228–10240, https://doi.org/10.1021/acsnano.1c02340.

63. J. Vavra, T. Shen, D. Stoian, V. Tileli, and R. Buonsanti, "Real-Time Monitoring Reveals Dissolution/Redeposition Mechanism in Copper Nanocatalysts During the Initial Stages of the CO_2 Reduction Reaction," *Angewandte Chemie International Edition* 60 (2021): 1347–1354, https://doi.org/10.1002/anie.202011137.

64. K. I. Popov, J. D. Trnjančev, and M. G. Pavlovic, "Dendritic Electrocrystallization and the Mechanism of Powder Formation in the Potentiostatic Electrodeposition of Metals," *Journal of Applied Electrochemistry* 11 (1981): 239–246, https://doi.org/10.1007/BF00610985.

65. P. V. Dudin, P. R. Unwin, and J. V. MacPherson, "Electrochemical Nucleation and Growth of Gold Nanoparticles on Single-Walled Carbon Nanotubes: New Mechanistic Insights," *The Journal of Physical Chemistry C* 114 (2010): 13241–13248, https://doi.org/10.1021/jp1043706.

66. H. E. M. Hussein, H. Amari, B. G. Breeze, R. Beanland, and J. V. MacPherson, "Controlling Palladium Morphology in Electrodeposition from Nanoparticles to Dendrites: Via the Use of Mixed Solvents," *Nanoscale* 12 (2020): 21757–21769, https://doi.org/10.1039/D0NR05630H.

Supporting Information

Additional supporting information can be found online in the Supporting Information section.